THE JOURNAL OF PHYSICAL CHEMISTRY C
A JOURNAL OF THE AMERICAN CHEMICAL SOCIETY

pubs.acs.org/JPCC
Article

Synthesis, Structures, Chemical Bonding, and Properties of $Al_{9-x}Fe_xMo_3$ with $0.5 \leq x_{Fe} \leq 1.8$

Marcel Dürl, Ruiwen Xie, Martin Panthöfer, Hongbin Zhang, and Angela Möller*

Cite This: J. Phys. Chem. C 2025, 129, 14167−14176
Read Online

ACCESS | Metrics & More | Article Recommendations | Supporting Information

ABSTRACT: We report the crystal structure and properties of the $Al_{9-x}Fe_xMo_3$ phases. Samples with nominal x_{Fe} content up to 2.5 were synthesized by arc-melting and annealed at 600 °C. The products were analyzed by ex situ and in situ X-ray diffraction, and the phase compositions were determined. The crystal structures of the ternary phases were refined at room temperature. The τ_1 phase, $Al_{8.5}Fe_{0.5}Mo_3$, crystallizes in the tetragonal Al_3Ti type of structure, whereas an orthorhombic distorted structure is observed for $Al_{9-z}Fe_zMo_3$ with $1.0 \leq z_{Fe} \leq 1.8$. At temperatures around ≈300 °C, a reversible orthorhombic ↔ tetragonal phase transition occurs. The τ_2 phase (disordered W-type of structure) is metastable at room temperature and decomposes above ≈425 °C into the Fe-enriched orthorhombic $Al_{9-z}Fe_zMo_3$ phase, AlFe, and $AlMo_3$. DFT calculations of the formation energies of Fe_{Al} substitution are reported, and aspects of chemical bonding in $Al_{9-x}Fe_xMo_3$ are provided (DOS, COHP, and ELF). The physical properties are investigated by ^{57}Fe-Mössbauer spectroscopy and magnetic measurements, indicating spin glass behavior at low temperatures.

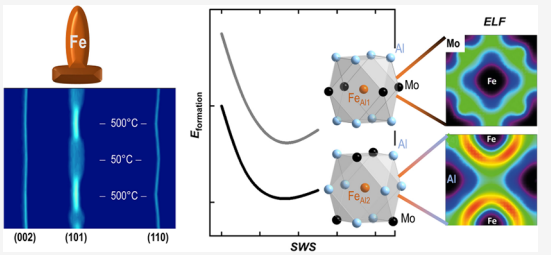

INTRODUCTION

Intermetallic binary phases (Al−Fe, Al−Mo, and Fe−Mo systems)[1−5] have been of considerable interest in the past decades due to their structural peculiarities and corrosion resistance. However, these materials are often brittle at room temperature and difficult to process for applications. Therefore, it has been of interest to elucidate ternary intermetallic compounds to improve material performance. The inherent physical properties of these phases are linked to the electronic aspect of strong hybridization of s,p-orbitals (here, Al) with d-orbitals of the transition metal (here, Fe and Mo).[6,7] Therefore, it is of interest to gain further insights into the chemical bonding of such ternary phases and to develop an understanding of the Fe_{Al} content in $Al_{9-x}Fe_xMo_3$ phases.

The ternary phase diagram Al−Fe−Mo has been mainly studied experimentally at temperatures above 800 °C and by thermodynamic modeling (CALPHAD, CALculation of PHAse Diagrams).[8−12] Two ternary phases have been reported, Al_8FeMo_3 (τ_1) and AlFeMo (τ_2). The latter crystallizes in a disordered W-type of compound with a significant compositional width of ≈±10 at % per element. The τ_2 phase forms above 1100 °C and is metastable at room temperature. It decomposes upon cooling into the τ_1 phase, AlFe, and $AlMo_3$ in an eutectoid reaction.[8] Ab initio calculations indicate that the τ_2 phase is stable at high temperatures in the presence of excess AlFe.[11] However, the presence of the τ_2 phase has been questioned, while the τ_1 phase has been observed up to 1450 °C.[12] Comparing the composition of the reported tetragonal τ_1 phase (Al_3Ti type)[8,12] calls for further investigations of the Fe content and site preferences. In particular, we are interested in the formation energies of Fe substitution on Al sites. In an earlier work, we reported the low Fe-content phases $Al_{9-x}Fe_xMo_3$ with $x_{Fe} \leq 0.9$ and showed the absence of Al_8Mo_3 above $x_{Fe} \approx 0.4$.[13] The question now arises about the maximum Fe content of the so-called τ_1 phase. Concomitantly, it implies an increasing average electron count, which might destabilize the tetragonal structure. Recently, a metastable orthorhombic phase has been shown to exist in the Al−Mo−Ti system and discussed with respect to strain and elastic instability.[14] This motivated us to probe for a relationship between the Fe content and chemical bonding in $Al_{9-x}Fe_xMo_3$. The second aspect of interest relates to the physical properties of these intermetallic phases.

This paper is organized as follows: (i) structural characterization of the $Al_{9-y}Fe_yMo_3$ (tI) and $Al_{9-z}Fe_zMo_3$ (oI) phases obtained from arc-melting and annealing, and the nominal Fe content used for the respective synthesis is given as x_{Fe} and presents the sample labeling as well; (ii) the section on quantum chemical calculations examines the formation energies for site-specific $Fe_{Al1,2}$ substitutions and addresses the chemical bonding situation in $Al_{9-x}Fe_xMo_3$; (iii) extended

Received: May 4, 2025
Revised: July 1, 2025
Accepted: July 9, 2025
Published: July 23, 2025

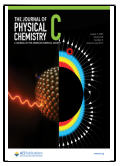

https://doi.org/10.1021/acs.jpcc.5c03044
J. Phys. Chem. C 2025, 129, 14167−14176

defects at interfaces are investigated by AC- and DC-magnetization measurements; and (iv) disordered fractions related to strain effects in domains and inherent electronic properties of iron in $Al_{9-x}Fe_xMo_3$ samples are probed by the local method of Mössbauer spectroscopy.

METHODS AND MATERIALS

Synthesis and Characterization. $Al_{9-x}Fe_xMo_3$ was prepared by arc-melting by using a custom-built arc furnace equipped with a nESSy TIG 172 DIC power source and a tungsten cathode. The copper plate of the arc furnace was continuously water-cooled to maintain thermal stability. Prior to melting, the metal wires were cleaned ultrasonically by sequentially washing them once with technical-grade acetone, ethyl acetate (Fisher Chemicals, ≥99.8%), and high-purity acetone (Fisher Chemicals, ≥99.8%). The compounds (pellets of ≈3 g) were synthesized in a two-step procedure: (i) AlFe from Al (Chempur, 99.5%, wire, Ø = 2 mm) and Fe (Alfa Aesar, 99+%, wire, Ø = 1.2 mm) in a 1:1 ratio and (ii) $Al_{9-x}Fe_xMo_3$ from AlFe, Al, and Mo (Chempur, 99.95%, wire, Ø = 1 mm) in stoichiometric ratios, resulting in nominal x_{Fe} ranging from 1.0 to 2.5. Typically, each pellet was melted 11 times. Samples of the 'annealed' $Al_{9-x}Fe_xMo_3$ series were obtained in evacuated silica ampules at 600 °C for 48 h. Pellets were cut into pieces and used for magnetic property measurements (Quantum Design Physical Property Measurement System, PPMS) in the temperature range of 1.8−300 K in applied magnetic fields up to ±8 T (DC). Zero field data were recorded after demagnetization procedures at 300 K; see the SI for details. AC measurements were conducted using H_{AC} = 1.587 Oe. Samples for X-ray powder and Mössbauer spectroscopic measurements were obtained by grinding small pieces to a fine and homogeneous powder.

X-ray diffraction data were recorded in transmission mode on a Stoe STADI P diffractometer with Mo Kα_1 radiation (λ = 0.70930 Å), a Ge(111) monochromator, and a MYTHEN 1 K detector (Dectris). Continuous scans: 2Θ step size of 0.015° in the 2Θ range from 1.500 to 73.485°. All samples were prepared as finely ground powder in paraffin oil between poly(vinyl acetate) foils. Full-pattern profile analysis (Rietveld refinements) was performed using Topas Academic V7,[15] applying the fundamental parameter approach.[16] Anisotropic line broadening due to spontaneous strain was modeled using Stephens' approach[17] as built in Topas Academic.[15] The τ_2 phase is reported as nonstoichiometric. Therefore, the starting composition of the τ_2 phase was taken as the initial composition of the melt (nominal $Al_{9-x}Fe_xMo_3$) and then approximated from the change of relative phase amounts before and after annealing. In situ experiments were performed under an inert gas atmosphere in a tube furnace (HT2, STOE & CIE GmbH, Darmstadt) with the sample contained in silica glass capillaries.

^{57}Fe Mössbauer spectra were recorded in transmission geometry using finely ground powdered samples dispersed in paraffin (mp 40−42 °C). All samples were checked for magnetic impurities (iron oxides) in the velocity range of −10 to 10 mm/s. Ambient temperature spectra were recorded in a magic angle setup to eliminate line asymmetry due to texture. Low-temperature spectra were recorded using a Montana C2 closed-cycle cryostat, in which the samples were contacted thermally using a brass sample holder. All Mössbauer spectra were calibrated relative to α-Fe. Data evaluation was performed using the Recoil software package.[18]

Quantum Chemical Calculations. The calculations on the thermodynamic stability and the density of states (DOS) were conducted using the exact muffin-tin orbitals (EMTO) method.[19] The Perdew−Burke−Ernzerhof (PBE) exchange−correlation functional[20] was employed for self-consistent calculations and, on top, for the full-charge density corrections to the total energies. The one-electron Kohn−Sham equations were solved with s, p, d, and f orbitals included in the basis set. A total of 7937 k points were sampled in the irreducible Brillouin zone. Regarding the $Al_{9-x}Fe_xMo_3$ compound, Fe was assumed to distribute randomly on the Al sites, for which the coherent potential approximation (CPA) was adopted.[21] Moreover, we calculated the total energies of $Al_{9-x}Fe_xMo_3$ (x_{Fe} = 0.5, 1.0, 1.5, and 2.0) under both ferromagnetic (FM) and paramagnetic (PM) states. In terms of the simulation on the PM state, the disordered local moment (DLM) model was applied,[22] in which the local magnetic moment was preserved, while the total magnetization summed up to zero by randomly assigning half of the Fe with spin-up and the other half with spin-down moments. The calculation of electron localization functions (ELFs)[23] was performed at the nonmagnetic state with a k-mesh of 12 × 12 × 6 using the Vienna Ab initio Simulation Package (VASP) and implementing the PBE exchange−correlation functional. The chemical orbital Hamilton population (COHP) was obtained using the LOBSTER code,[24] providing an atomic picture of the bonding characters among the atoms.

RESULTS AND DISCUSSION

Structural Characterization. The tetragonal body-centered Al_3Ti-type structure (tI) consists of two crystallographic sites for Al: Al1 (2b) and Al2 (4d), as shown in Figure 1. The nearest neighbor environments of the two Al sites differ with respect to a square-planar or tetrahedral $AlMo_4$ arrangement. In this work, we study the substitution of Al by Fe focusing on site preferences and implications on bonding below.

For simplicity, we will use the formula $Al_{9-x}Fe_xMo_3$ for which we give the nominal Fe content as x_{Fe} = 1.0, 1.25, 1.5,

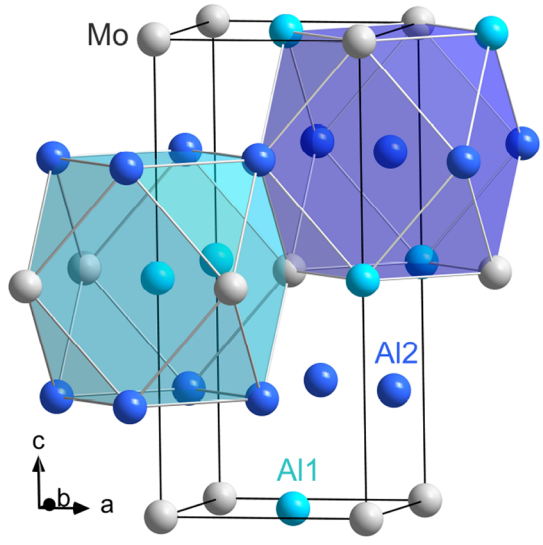

Figure 1. Crystal structure of the tetragonal phase (Al_3Ti type). The $Al(Al_8Mo_4)$ polyhedra for the two Al sites (Al1, 2b and Al2, 4d) are shaded.

https://doi.org/10.1021/acs.jpcc.5c03044
J. Phys. Chem. C 2025, 129, 14167−14176

1.75, 2.0, 2.25, and 2.5 used in arc-melting synthesis according to the stoichiometry given in eq 1.

$$x\mathrm{AlFe} + (9 - 2x)\mathrm{Al} + 3\mathrm{Mo} \rightarrow \mathrm{Al}_{9-x}\mathrm{Fe}_x\mathrm{Mo}_3 \quad (1)$$

We present the characterization of as-synthesized and annealed samples by analyzing our X-ray diffraction data at room temperature, with further details provided in the Methods and Materials section and the SI. Here, we address the following issues with respect to the nominal $Al_{9-x}Fe_xMo_3$ samples: (i) the stability range of the ternary intermetallic phase (τ_1) depending on x_{Fe}, (ii) the orthorhombic distortion (oI) of the tetragonal phase (tI) upon Fe substitution, (iii) the iron site preferences, and (iv) the total Fe content for oI and tI.

In Figure 2, we show the powder diffraction data for as-synthesized and annealed samples of the nominal composition $Al_{9-x}Fe_xMo_3$ ($1.0 \leq x_{Fe} \leq 1.75$), see eq 1. Fully refined XRD data and analytic results are provided in the SI for all of the studied samples. We first discuss the top two panels of Figure 2 for nominal $x_{Fe} = 1.0$. In comparison, the as-synthesized sample contains a larger fraction of the tetragonal phase (tI) than the annealed one. For the latter, an orthorhombic distortion is clearly indicated by the splitting of Bragg reflections, see marked boxes for (011) and (101) in Figure 2. However, note that both phases (tI and oI) are present. Figure 3 provides the phase fractions of these two modifications and informs about the presence of side products upon substitution. Explicitly, for $x_{Fe} = 1.0$, the tI and oI phases are contained in equal fractions (≈45 wt %) in the as-synthesized sample, contributing to the broadening of the marked reflection(s). This changes upon annealing to ≈64%-wt oI and 27%-wt tI. While the relative fraction of tI remains roughly constant throughout the series, the oI fraction depends on x_{Fe} up to $x_{Fe} \approx 1.75$ and then remains constant.

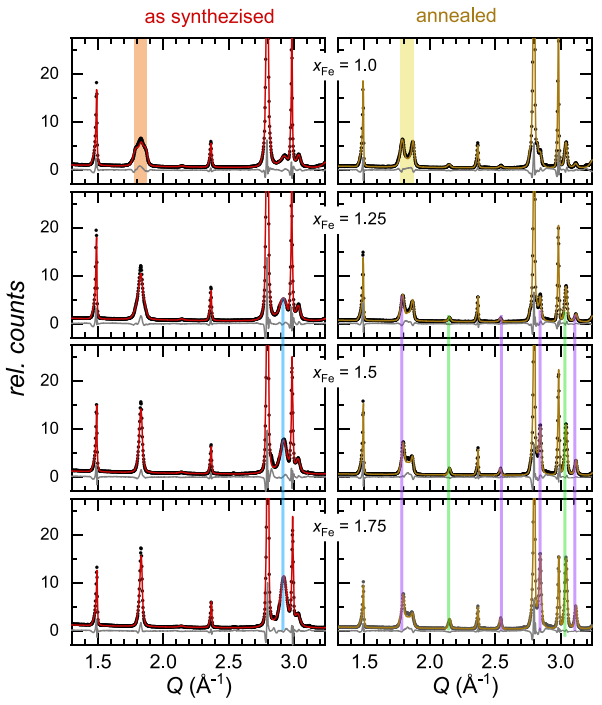

Figure 2. Room-temperature powder X-ray diffraction data for the series $Al_{9-x}Fe_xMo_3$ with nominal x_{Fe}. Experimental (black), calculated (red, as-synthesized; brown, annealed), and difference (gray) data. Contributions to the diffraction pattern are marked by vertical lines: τ_2 (blue), $AlMo_3$ (purple), and AlFe (green). Top panels: orange and yellow shaded areas indicate tetragonal and orthorhombic distortions of the parent Al_3Ti type of structure.

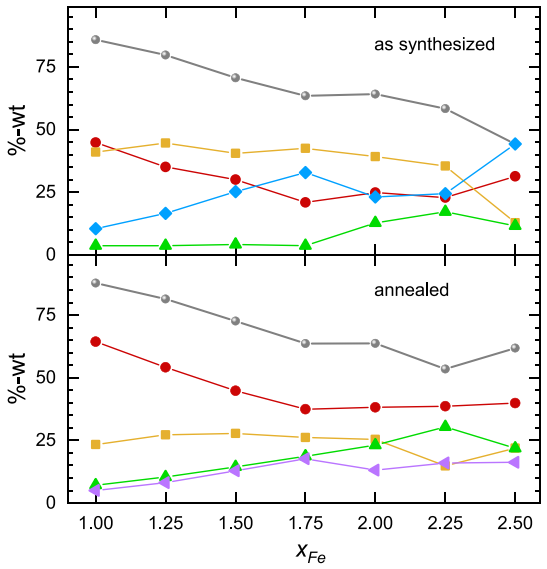

Figure 3. Refined phase compositions for the nominal x_{Fe} samples. The phases are given individually for tI (yellow) and oI (red), as well as their total content (gray). Side products are τ_2 (blue), AlFe (green), and $AlMo_3$ (purple).

Figures 2 and 3 provide information about the side products formed in the synthesis. For the nominal Fe content, $x_{Fe} \geq 1.0$, we observe an increase of the τ_2 phase (average composition: $Al_{0.3(1)}Fe_{0.4(1)}Mo_{0.30(1)}$, a = 3.037(3) Å) as a side product obtained from the rapid cooling of the melt (arc-melting). Concomitantly, the oI phase fraction decreases according to our ex situ X-ray diffraction data analysis. This implies that the disordered τ_2 phase contains the excess Fe content that is not transforming into the oI phase under arc-melting conditions.

After annealing, both polymorphs (tI with $Al_{9-y}Fe_yMo_3$ and oI with $Al_{9-z}Fe_zMo_3$), respectively, exist at room temperature along with the products from the decomposition of τ_2. Notably, the fraction of the oI phase surpasses the tI one, pointing out that the oI phase is associated with a higher Fe content ($1.0 \leq z_{Fe} \leq 1.8$) stemming from the decomposition of the τ_2 phase. It appears that tI is approximately a line phase, as y_{Fe} remains close to 0.5 for Fe_{Al2}, irrespective of the synthesis protocol. Therefore, Fe-site occupancies (given in Figure 4 and the SI) will be relevant and discussed further in relation to the formation energies and physical properties below.

Next, we discuss the orthorhombic splitting (oI), which deviates approximately ±0.1 Å from the mean a-lattice constant (3.75 Å) of the tI phase; see the SI for refined lattice constants. Interestingly, this deviation remains almost constant for nominal $x_{Fe} \geq 1.5$. The same holds for the c-lattice constant of the oI phase (8.40 Å), which is slightly smaller than $c \approxeq 8.41$ Å for tI. The overall c/a ratio is almost equal and constant for both phases. With respect to the apparent distortion (oI), we suggest that (i) increasing the Fe substitution on Al1 sites removes the 4-fold symmetry, possibly caused by increasing antibonding Fe−Mo interactions within the a,b-plane and (ii) stronger hybridization of Fe with surrounding Al sites exists for Fe substituting the Al2 position. Both aspects of chemical bonding are further discussed below. The case (ii) finds its representation by a smaller c^{oI}-lattice

https://doi.org/10.1021/acs.jpcc.5c03044
J. Phys. Chem. C 2025, 129, 14167−14176

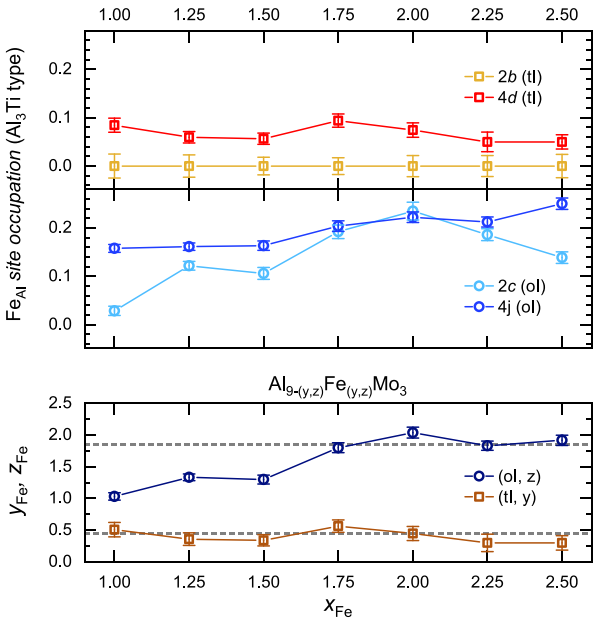

Figure 4. Occupation factors from Rietveld refinements of room-temperature powder X-ray diffraction data for the annealed series given for the parent Al_3Ti type of structure. Top panel: tI (orange, red); oI (light blue, blue). Bottom panel: total composition of $Al_{9-(y,z)}Fe_{(y,z)}Mo_3$: y_{Fe}(tI) and z_{Fe}(oI). Dashed gray lines serve as a guide to the eye.

constant. More important is the higher Fe content on the Al2 site, Wyckoff position (4*j*), for which the z/c^{oI} parameter deviates from the special 4*d* site $z/c^{tI} = 1/4$. For the sake of a stable multiphase refinement, we kept initially $z/c = 1/4$ for both oI and tI. In order to avoid significant correlations in the refinements, we determined afterward the z/c^{oI} parameter for the annealed phases and obtained, e.g., 0.2468(4) Å for $x_{Fe} = 1.75$. This value is well in line with the reported one for the $D0_{22}'$ phase existing in the ternary Al−Mo−Ti system.[14]

In situ X-ray diffraction data are provided in Figure 5 for the $x_{Fe} = 1.0$ case. Around 300 °C, the oI phase transforms reversibly into a high-temperature tetragonal phase ($Q \approx 1.85$, 3.35, and 4.5 Å^{-1}). The τ_2 phase vanishes at temperatures above 425 °C ($Q \approx 2.9$ Å^{-1}), yielding mainly AlFe and $AlMo_3$, while excess iron supplements the annealed oI phase $Al_{9-z}Fe_zMo_3$ with $z_{Fe} \leq 1.8$. This implies that the oI phase rapidly approaches the maximum Fe content with annealing temperatures already around 500 °C. This temperature seems well in line with the bulk diffusion temperatures of sufficiently mobile atoms, 275 °C for Al and 631 °C for Fe. Inherent to nonequilibrium thermodynamics is material transport via diffusion processes.[25,26] Spinodal decompositions and/or coalescence (τ_2) may lead to lamellar structures with increased defect sites at interfaces upon rapid cooling. Diffusion at surfaces is linked to the Hüttig temperature, 165 °C for Al and 270 °C for Fe. These indicate that the defect concentrations at interfaces are reduced upon annealing at moderate temperatures. Thereby, the strain between adjacent phases is also minimized. Interestingly, the oI ↔ tI phase transition around 300 °C falls into this temperature regime. It is observed that the orthorhombic low-temperature phase is obtained with almost constant lattice parameters (oI) for the entire substitution series after initial annealing (Figure 2) and multiple temperature cycling protocols (Figure 5). We emphasize that the structural phase transition belongs to the class of group (tI, *I*4/*mmm*)−subgroup (oI, *I*/*mmm*) relationships, for which a continuous phase transition of second order is allowed.[27,28]

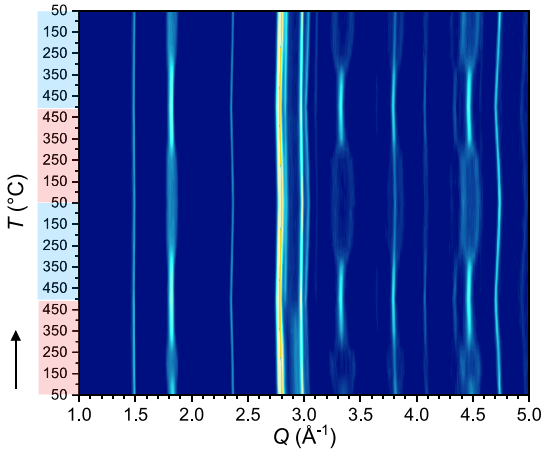

Figure 5. Contour plot of an in situ X-ray powder diffraction pattern of nominal, as-synthesized Al_8FeMo_3, showing the oI ↔ tI transition and the decomposition of the τ_2 phase. Light red (heating) and pale blue (cooling) boxes serve as a guide to the eye, and the arrow indicates the direction of the temperature change.

We conclude our phase analysis with the important aspect that Al sites are preferably substituted by Fe in the tI and oI phase, giving rise to $y^{tI} \neq x_{Fe}$ and $z^{oI} \neq x_{Fe}$. We address this by the refinement of occupation factors for the annealed samples, with experimental results provided in Figure 4. The occupation factors for Al1 (2*b*) and Al2 (4*d*) refer to the Al_3Ti type of structure depicted in Figure 1 for the tI phase and oI using $a \neq b$ and (Al1:2*c*, Al2:4*j*). We take note that for tI, only the Al2 site gets populated and is represented by $y_2 \approx 0.5$ for both as-synthesized and annealed samples. Contrarily, Fe substitution occurs on both Al sites in the oI phase in accordance with the higher Fe content. This can be seen by an increasing occupancy of the Al1 site with Fe, reaching a maximum content of $z_1 \approx 0.6$. The occupancy of the Al2 site slightly increases from $z_2 = 1.0$ to 1.2 at the saturation limit, which gives $z_1 + z_2 = z_{max} \lessapprox 1.8 \lessapprox x_{Fe}$. Beyond $x_{Fe} = 1.75$, the oI phase is limited to z_{max}, which also finds support from constant lattice parameters. In conclusion, the maximal Fe_{Al} substitution—in particular, on the Al1 site—points to the origin of the apparent orthorhombic distortion below 300 °C. Next, we investigate the formation energy for the substitution of Al with Fe.

Theory. In order to understand the site preference of the $Fe_{Al1,2}$ substitution and the limiting occupation factors, we evaluate the thermodynamic stability of $Al_{9-x}Fe_xMo_3$ (x_{Fe} = 0.5, 1.0, 1.5, 2.0) by calculating the formation energy with respect to the stable single phases using the EMTO method. To facilitate the theoretical work, we explicitly use the tetragonal structure for reference. In order to simulate the chemical disorder with Fe doping with simultaneously high accuracy and low computational cost, the coherent potential approximation (CPA), as implemented in the EMTO code, is adopted. Additionally, the paramagnetic state is approximated by the disordered local moment (DLM) state,[29,30] in which the local magnetic moment of each atomic site is preserved, while the total magnetization is ensured to be zero by randomly assigning 50% of Fe with spin-up and spin-down moments,

https://doi.org/10.1021/acs.jpcc.5c03044
J. Phys. Chem. C 2025, 129, 14167−14176

respectively. In this regard, the DLM state is a more realistic approximation to the paramagnetic state as compared to the nonmagnetic state.

Here, we take the approach that x_{Fe} presents the Fe_{Al} occupancy either on the Al1 or Al2 site, respectively, see Figure 6. As an example, for $Al_{8.5}Fe_{0.5}Mo_3$, the structure with c/a = 2.22 at SWS = 2.91 Bohr possesses the lowest energy with Fe occupying the Al2 site at the paramagnetic DLM state, slightly lower than that of Fe on the Al1 site. The Wigner–Seitz radius (SWS) is defined as $V = \frac{4}{3}N\pi SWS^3$, in which N is the total number of atomic sites and V is the total volume of the simulation cell. Accordingly, the formation energies are depicted as functions of the SWS in Figure 6. The minimum of each curve corresponds to the lowest total formation energy. It should be noted that the calculated c/a values are in reasonable agreement with experimental data $c/a \approxeq 2.23(2)$ for the entire series.

It can be observed from Figure 6 that nominal Al_8FeMo_3 with Fe located solely on the Al2 site (DLM state) exhibits the lowest global formation energy at around −0.026 Ry/site. This is in excellent agreement with our experimental observation of the $z_2 \approx 1.1(1)$ limit for the oI phase. It is worth mentioning that for Fe_{Al1}, the lowest global formation energy is calculated for x_{Fe} = 0.5. This corresponds nicely to $z_1 \approx 0.6$ for maximal occupancy for the oI phase from experiments. For the tI phase, y_2 = 0.5 is experimentally observed, but not the theoretical value for x_{Fe} = 1.0 exclusively at the Al2 site, compare Figure 4 with Figure 6 left panels. Hence, the tI (τ_1) phase has the composition $Al_{8.5}Fe_{0.5}Mo_3$. Contrarily, the oI phase is well represented by $z_2 \approx 1.0$ at the Al2 site, e.g., the global formation minima of our calculation. The occupancy with $z_1 \approx 0.5$ at the Al1 site (experiment, oI) is at higher formation energies. It is tempting to link the latter to the experimental observation of a symmetry reduction, i.e., the structural motif of the planar square to rectangular Fe_{Al1}–Mo_4 arrangement. In comparison, the pseudotetrahedral Fe_{Al2}–Mo_4 arrangement is clearly preferred with $z_2 \approx 1.0$ according to our calculations and in agreement with the experimentally highest overall substitution, yielding $Al_{7.2}Fe_{1.8}Mo_3$. In order to remind the reader of the close relationship between the tetragonal and orthorhombic phases, we recall the reversible oI ↔ tI transition (Figure 5) at very moderate temperatures. We estimate the small enthalpy change of ≈3 J/g from DSC measurements upon cooling.

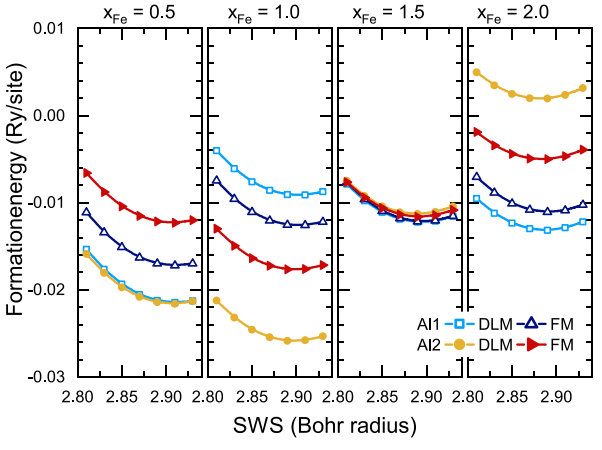

Figure 6. Formation energy as a function of the Wigner–Seitz radius (SWS) for $Al_{9-x}Fe_xMo_3$ with Fe occupying exclusively the Wyckoff positions Al1 (2*b*) and Al2 (4*d*) of the tI phase (Al_3Ti type of structure), respectively. Calculations for Fe contents (x_{Fe} = 0.5, 1.0, 1.5, and 2.0) were done at paramagnetic (DLM) and ferromagnetic (FM) states.

Next, we explain by evaluation of the formation energies that phases with Fe doping concentration x_{Fe} significantly larger than 1.0 are not thermodynamically stable. The preferred Fe occupation site changes from Al2 to Al1 for high Fe content (Figure 6, right panels). The formation energy (DLM calculation) of a theoretical $Al_7Fe_2Mo_3$ compound with Fe located at Al1 sites is around −0.012 Ry/site, which is 0.014 Ry/site higher than that of $Al_8Fe_1Mo_3$ with Fe located at Al2 sites as the thermodynamically stable phase. For example, the hypothetical $Al_7Fe_2Mo_3$ will decompose based on the formation energy of ≈0.88 mRy/site with respect to the experimentally observed phases: $Al_{7.5}Fe_{1.5}Mo_3$, AlFe, and $AlMo_3$. For reference, we show in Figure 6 the calculations for the ferromagnetic (FM) state. It is worth mentioning that for none of the presented cases, does a thermodynamically stable FM ground state exists.

In order to understand the Fe-site preference for the Al2 site, we further analyzed the electron localization function (ELF) for the two Al sites. ELF has been proposed to aid in the analysis of the chemical bond.[23] We chose the comparison of hypothetical Al_9Mo_3 with $Al_{7.5}Fe_{1.5}Mo_3$. For the latter, the formation energies for x_{Fe} = 1.5 at Al1 and Al2 sites are almost equal, see Figure 6. For a homogeneous electron gas, ELF holds the value of 0.5 and will have its highest value (→1) with maximum electron localization. The latter suggests strong and localized electron pairs. As demonstrated in Figure 7a for the hypothetical Al_3Mo compound (Al_3Ti type of structure), the highest ELF value is found within the planes solely decorated by Al2. By substitution of Al1 with Fe (see Figure 7b), plane (1) becomes much more delocalized. Similarly, but to a lesser extent, this holds for planes (2) and (4) as well. In contrast, when Fe occupies the Al2 site, the electron localization still persists, as observed from the ELF of plane (4) in Figure 7c. Therefore, compared to the strong electron delocalization for Fe_{Al1}, Fe prefers to occupy the Al2 site, as the interaction between Fe and its surrounding atoms is relatively higher. However, upon further increasing x_{Fe} at the Al2 site, the electron delocalization behavior would eventually dominate. To supplement our analysis, we provide the ELF contour plots for the (010) plane in the SI.

Further insights into the chemical bonding from the analysis of projected crystal orbital Hamilton populations (p-COHP) are provided in the SI for $Al_{9-x}Fe_xMo_3$ with x_{Fe} = 0.75 and 1.5. Here, we briefly summarize these results. Around the Fermi energy, Fe → Al2, Fe → Mo, and Mo → Al1 interactions are antibonding. At energies $E - E_f \approx -2$ eV, these three interactions are bonding. The main difference between Fe_{Al1} and Fe_{Al2} is observed for an enhanced hybridization of the latter with Al1, which even develops into a bonding situation at E_f for $x_{Fe} \ll 1.5$. Interestingly, for x_{Fe} = 1.5, the Mo → Al2 (Fe-substituted Al2 layers) interaction turns antibonding around −2 eV. This is in agreement with the higher formation energy for Fe_{Al2} and supports the above derived maximum occupancy of ≈1.0. To conclude, we emphasize that for all nearest neighbor interactions not explicitly discussed above, metallic scenarios apply with a large dispersion of electronic bands.

Additionally, we like to emphasize that by analyzing the density of states (DOS), we find a high density of states at E_f

https://doi.org/10.1021/acs.jpcc.5c03044
J. Phys. Chem. C 2025, 129, 14167−14176

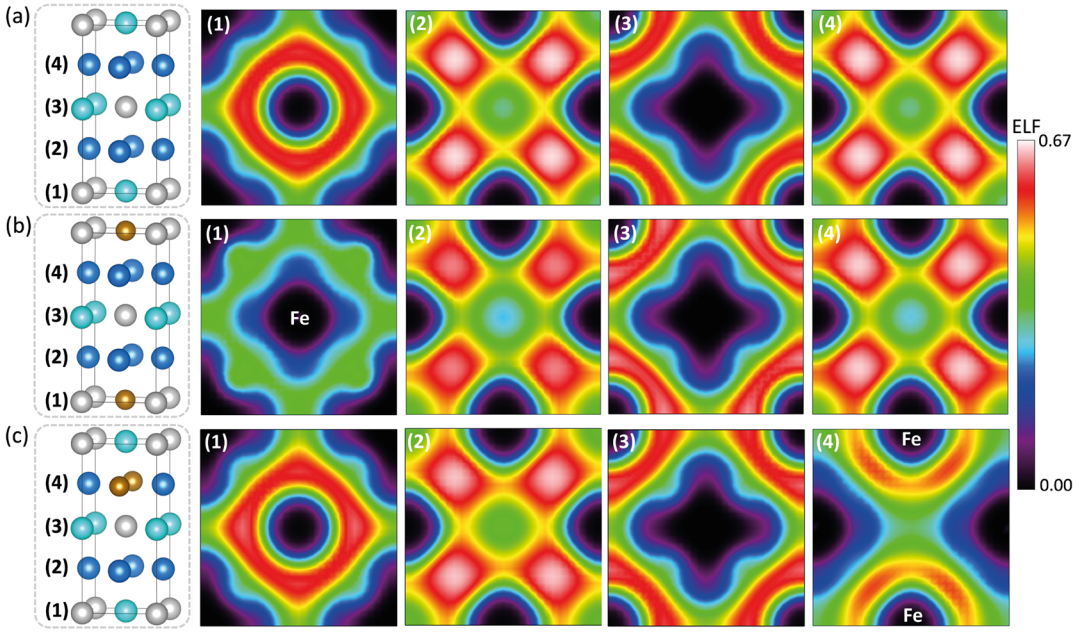

Figure 7. Planar contour plots of the electron localization function (ELF) calculated for the Al_3Ti structure type in (a) hypothetical Al_3Mo, (b) $Al_{7.5}Fe_{1.5}Mo_3$ with Fe occupying the Al1 site, and (c) $Al_{7.5}Fe_{1.5}Mo_3$ with Fe occupying the Al2 site. The numbers in brackets from (1) to (4) label the (001) planes in the crystal structures displayed in the left panel, Mo(gray), Al1 (light blue), Al2 (dark blue), and Fe (orange).

with pronounced Fe d-orbital contribution, see the SI. Therefore, the magnetic properties will be dominated by iron in its three environments: Fe_{Al1} or Fe_{Al2}, respectively, each separated by nonsubstituted layers, and adjacent layers partially occupied by Fe. These possibilities refer to tI and oI phases and present a scenario of so-called impurity spins in a metal with variable interatomic distances. This suggests the applicability of the RKKY model[31−33] for the magnetic properties of $Al_{9-x}Fe_xMo_3$.

Magnetic Properties. The magnetic properties of as-synthesized and annealed $Al_{9-x}Fe_xMo_3$ samples are investigated; see also the SI for further details. In Figure 8, we present the field-dependent magnetization data at 1.8 K, for which we show $M(H)$ per iron (x_{Fe}). For reference, we include the data for as-synthesized AlFe. In the latter, the magnetic moment is small and contributes only in a typical Pauli paramagnetic fashion. Both side products, FeAl and the disordered τ_2 phase, contain Fe in a cubic surrounding of

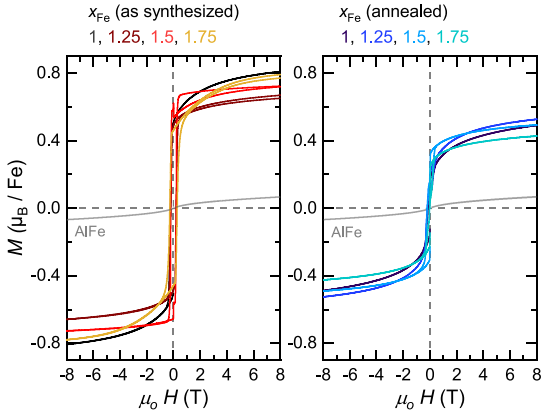

Figure 8. Field-dependent magnetization of as-synthesized (left) and annealed (right) $Al_{9-x}Fe_xMo_3$ samples at 1.8 K. Dashed lines are a guide for the eye.

nearest neighbor atoms. Thus, we assume that these two Fe-containing phases contribute with rather similar and very low total magnetic moments to our $M(H)$ data. Neither of these side products nor $AlMo_3$ seems to have a significant impact on the magnetization as a function of their phase fractions, see Figure 8 in comparison with their weight percentages provided in Figure 3. Therefore, we discuss the main features of the data presented in Figure 8 relating to the tI and oI phases in the context of as-synthesized and annealed samples.

As-synthesized samples exhibit paramagnetic $M(H)$ curves above 100 K and develop increasing remanence, as well as coercive fields, at lower temperatures (see the SI). In Figure 8 (left), a clear hysteresis with $\mu_0 H_c \approx \pm 0.23$ T is observed at T = 1.8 K. This feature is less pronounced (smeared out) for the annealed samples, for which spontaneous polarization of magnetic moments for small applied magnetic fields also occurs, see Figure 8 (right). In comparison, the average magnetic moments reach $\approx 0.7(1)$ μ_B at 8 T for the as-synthesized samples, while the lower values of about 0.5 μ_B are observed for the annealed ones. Thus, we were interested in evaluating the effect of disordered local moments at Fe sites in the intermetallic tI and oI phases. The indirect exchange of localized spins through conduction electrons (RKKY model)[31−33] represents the situation of alternating ferromagnetic and antiferromagnetic coupling, an essential aspect of spin glasses.[34] Since our samples are not single phase, a second aspect might be of relevance, especially at domain boundaries, effectively inducing pinning effects.[35,36]

We start with the temperature dependence of the AC susceptibility and DC magnetization for x_{Fe} = 1.25 as an example, see Figure 9. $M(T)$ data are depicted in the panels on the right for the as-synthesized and annealed samples. These reveal signatures of a spin glass (SG) indicated by the deviation of zero field cooling (zfc) from field cooling (fc) data, which appear at small applied fields around 90 K (as-synthesized) and ≈60 K (annealed); see also the SI for further details. With increasing magnetic fields, the onset temperature, where

https://doi.org/10.1021/acs.jpcc.5c03044
J. Phys. Chem. C 2025, 129, 14167−14176

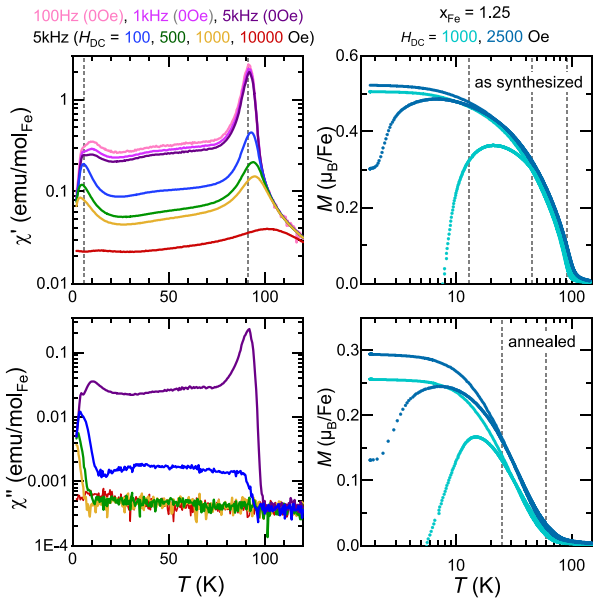

Figure 9. Left: AC susceptibility for the as-synthesized x_{Fe} = 1.25 sample. Right: the temperature-dependent DC magnetization is shown for the as-synthesized and annealed x_{Fe} = 1.25 samples. Measurements were taken in field cooling (line) and zero field cooling (circle) mode. Dashed lines serve as a guide to the eye.

$M_{fc}(T)-M_{zfc}(T)$ starts to diverge, shifts toward lower temperatures. This shift is larger for the as-synthesized sample in comparison with the annealed one.

In Figure 9 left, we show the AC susceptibilities for the as-synthesized x_{Fe} = 1.25 sample. At ≈92 K, features of an SG appear. In zero applied magnetic field, the peak maximum slightly shifts with increasing frequency to higher temperatures. For applied magnetic fields up to 100 Oe, this feature shifts to lower temperatures; see also $\chi''(T)$. Further increase in the applied magnetic fields reveals paramagnetic response for the imaginary part of the AC susceptibility down to ≈20 K. Interestingly, the maxima in $\chi'(T)$ around 90 K persist and smear out approaching H_{DC} = 10,000 Oe. It is tempting to assign this to the presence of ferromagnetic correlations.

Additionally, we observe a second feature in the $\chi'(T)$ data below 20 K. For H_{DC} = 0 Oe, a broad hump occurs around 10.0 K, which gradually decreases with higher frequency and merges with the asymmetric peak at lower temperatures. Both $\chi'(T)$ and $\chi''(T)$ clearly show pronounced maxima, which we assign to the freezing temperature T_f. This is corroborated by a slight shift toward higher temperatures with increasing frequency and the corresponding response to applied magnetic fields, T_f(5 kHz) ≈ 5.8 K (0 Oe) → 3.8 K (1000 Oe). Note that the phase transition from the SG into an ordered state, the frozen SG, is continuous. Taking the onset temperature from $\chi''(T)$ in the zero field, the transition possibly develops below 30 K.

In conclusion, we observe for the as-synthesized samples ferromagnetic correlations around 90 K and antiferromagnetic correlations below ≈5 K based on the overall shift of the respective maxima (χ') in applied magnetic fields. The intermediate temperature range then corresponds to an SG state. We probe this scenario by measuring the specific heat, see the SI. No λ-anomaly is observed, which indicates the absence of long-range magnetic order. A broad contribution related to the magnetic part of the total specific heat is observed in the low-temperature regime. The Debye temperature (≈440 K) used for the calculation of the phonon contribution agrees well with the published averaged values for Al, Fe, and Mo metals.[37]

In order to gain further insights into the differences between as-synthesized and annealed samples, we investigated the aspect of magnetic fluctuations and antisite disorder by the local probe of Mössbauer spectroscopy.

^{57}Fe Mössbauer Spectroscopy. Next, we investigate the as-synthesized and annealed samples by Mössbauer spectroscopy; see the SI for experimental data and evaluation of hyperfine parameters, including as-synthesized AlFe for reference. Note that the respective magnetic sextet spectra of α-Fe or iron oxides are absent for our samples.

The spectra were evaluated with respect to two paramagnetic doublets (sites 1 and 2), see Figure 10 (left). Note that these two sites represent Fe in disordered environments, including strain (site 1), while site 2 reflects the electronic situation governed by dominant 3p(Al)−3d(Fe) interactions in the intermetallic phases, not to be confused with the $Fe_{Al1,2}$ substitutions investigated above. We started with the hyperfine parameters at room temperature. First of all, we note that the two quadrupole splittings QS1 and QS2 are quite different, with average values of QS1 ≫ QS2. We take site 1 as a measure of disorder because of the decrease in relative Fe-site fractions (f_1) upon annealing when compared with their as-synthesized counterparts, see the SI. With increasing x_{Fe} up to 1.75, the ratio of f_1 to f_2 changes from approximately 1.0 to 0.7 for the as-synthesized and from 0.7 to 0.3 for the annealed samples at room temperature. For comparison, the respective ratio of 0.4 is observed for our as-synthesized AlFe, which indicates a disordered fraction being present.

The center shifts CS of the two doublets differ as well, which is again more pronounced for the as-synthesized samples. At room temperature, CS values between 0.22 and 0.26 mm/s are observed. This is in agreement with our as-synthesized AlFe

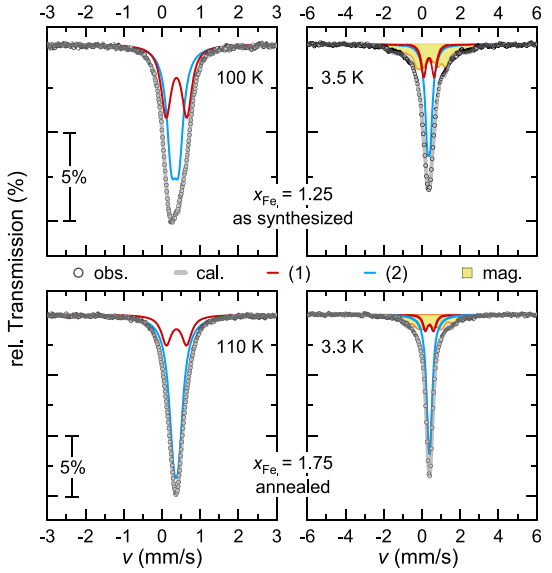

Figure 10. ^{57}Fe Mössbauer spectra for as-synthesized x_{Fe} = 1.25 (top) and annealed x_{Fe} = 1.75 (bottom) samples at selected temperatures above and below the onset of magnetic fluctuations. Experimental data (black circles), simulated spectra (gray), subspectra: site 1 (red), site 2 (blue), and magnetic (shaded orange).

https://doi.org/10.1021/acs.jpcc.5c03044
J. Phys. Chem. C 2025, 129, 14167−14176

sample and literature data.[38] It implies that Fe sites experience predominantly strong electronic hybridization with s,p-orbitals of Al. For comparison, CS values are reported around −0.23 mm/s for binary Fe−Mo phases, reflecting the opposite charge transfer on iron.[38] In other words, iron evades strong electronic interaction with Mo 4d-orbitals in $Al_{9-x}Fe_xMo_3$, in agreement with our findings from the calculations above. Interestingly, for the respective nominal defect contribution (site 1), lower *CS* values are observed for AlFe, while the respective CS1 shifts to higher values for $Al_{9-x}Fe_xMo_3$ samples.

On a different note, from CS(T) data, the second-order Doppler shift[39] associated with thermal vibrations of the ^{57}Fe nuclei can be obtained. We derive the Mössbauer specific Debye temperatures, $\theta_{M1} \approx 370$ and $\theta_{M2} \approx 395$ K, for the two Fe sites. The lower θ_{M1} also supports the assignment as a defect site as the surrounding lattice is slightly "softer".

In Figure 10, we present data for two nominal x_{Fe} samples at low temperatures. Hyperfine parameters for these selected examples are given in Table 1. The spectra were evaluated with respect to two paramagnetic doublets (sites 1 and 2) and the onset of magnetic fluctuations. The latter manifests initially by line broadening (site 1) below 75 K. In the case of the as-synthesized sample, gradually increasing site fractions of magnetically split Mössbauer spectra appear concomitantly toward lower temperatures. For the annealed sample, similar small hyperfine magnetic fields are observed below 10 K. Such small hyperfine magnetic fields of up to ≈75 kOe reveal significant broadening due to a nonstatic distribution of on-site H_{hf}, entering the experimental observation time scale of $\approx 10^{-8}$ s. All other site fractions fluctuate faster and thus appear still paramagnetic at around 3 K. It is interesting to note that sites 1 and 2 contribute at the lowest temperature roughly in equal site fractions to the magnetically split Mössbauer spectra. We emphasize that the ratios of the magnetic site fraction and the paramagnetic site fraction 2 are around 1:1 for the as-synthesized samples and 1:2 for the annealed samples at around 3 K. It is tempting to relate this to the differences in the total magnetization (Figure 8).

Our conjecture is that site 1 relates to disordered Fe atoms, which eventually freeze below 100 K. Possibly, these sites are located at phase boundaries (including local strain), which is in line with the larger QS1 value. Then, site 2 would represent the fraction of Fe atoms forming a random cluster glass with weak nearest neighbor spin alignment but absence of long-range ordering. Upon annealing, the f_2 fraction increases, which might point toward extended domains of the random cluster glass and diminishing phase boundaries and strain. However, the fact that both sites 1 and 2 develop magnetic fluctuations suggests that these two are correlated at low temperatures.

Table 1. Hyperfine Parameter for the Fe Sites (1, 2, Mag.) Denoted in Figure 10 for the As-Synthesized (x_{Fe} = 1.25) and Annealed (x_{Fe} = 1.75) Samples[a]

nom. x_{Fe}	Fe site	CS	QS, ϵ	f	H_{hf}	χ^2
1.25 (100 K)	(1)	0.380(2)	0.543(7)	43		0.88
	(2)	0.343(1)	0.192(3)	57		
1.25 (3.5 K)	(1)	0.359(6)	0.54(2)	19		0.75
	(2)	0.355(2)	0.163(9)	41		
	(mag.)	0.45(1)	0.023(8)	40	75(38)	
1.75 (110 K)	(1)	0.379(3)	0.528(5)	23		0.82
	(2)	0.3690(8)	0.129(2)	77		
1.75 (3.3 K)	(1)	0.383(9)	0.43(5)	11		0.75
	(2)	0.389(1)	0.10(1)	59		
	(mag.)	0.39(2)	0.028(7)	30	57(22)	

[a]CS (center shift), QS (quadrupol splitting), and ϵ (quadrupol shift) are given in units of mm/s, site fraction (f) in %, the magnetic hyperfine field (H_{hf}) in kOe, and χ^2 represents the quality of the fitted spectra.

CONCLUSIONS

$Al_{9-x}Fe_xMo_3$ samples with $1.0 \le x_{Fe} \le 2.5$ were synthesized by arc-melting. We identified two coexisting phases, $Al_{8.5}Fe_{0.5}Mo_3$ (tI) and $Al_{9-z}Fe_zMo_3$ (oI), with $1.0 \le z_{Fe} \le 1.8$. The former is assigned to a line phase. We show that for the latter phase, z depends on the initial nominal Fe-content x_{Fe} and increases upon decomposition of the metastable τ_2 phase (above 425 °C) during annealing procedures. With respect to the elastic properties of the oI phase, we observed a reversible oI ↔ tI phase transition around 300 °C. The tI and oI phases are different with respect to the substitution of Al sites by Fe: (tI) Fe_{Al2} only and (oI) Fe_{Al1} with z_1 up to 0.6 and Fe_{Al2} with $z_2 \le 1.2$. Experimental occupation factors and site preferences are in line with our calculated formation energies. An explanation of the thermodynamic stability for the Al2 site (x_{Fe} = 1.0) is derived from orbital-resolved DOS, ELF, and p-COHP calculations up to x_{Fe} = 1.5. The high density of states at the Fermi energy is dominated by Fe(3d orbitals) and Mo(4d orbitals) at a slightly higher energy. According to our p-COHP calculations, Mo → Fe interactions are antibonding at E_f. Contrarily, the s, p hybridization between Fe and Al is strong but larger when Fe substitutes the Al2 site. The dominant Al−Fe interaction is in agreement with the chemical shift obtained from our Mössbauer experiments.

The magnetic properties of the $Al_{9-x}Fe_xMo_3$ phases are of the glassy type. Below 100 K, remanence is observed for all samples from the $M(H)$ data. Only the as-synthesized samples exhibit nearly equal coercive fields at 1.8 K independent of x_{Fe}. In combination with Mössbauer spectroscopic investigations, we find significantly larger fractions of disordered Fe sites (associated with domain walls and strain) for the as-synthesized samples. We suggest that the density of these disordered Fe sites at interfacial surfaces (tI−oI) introduces pinning effects responsible for remanence and/or coercive fields. Mössbauer data provide further insights into the spin glass dynamics. We observe magnetic fluctuations gradually entering the time window of the experiment upon cooling. We emphasize that the disordered spins and an equal fraction of spins from the cluster glass are correlated below the freezing temperature. The magnetic hyperfine fields at our lowest experimental temperature are small and most importantly not static. Along with the absence of magnetic long-range order, the $Al_{9-x}Fe_xMo_3$ phases belong to the class of spin cluster glass interacting with interfacial defect sites.

ASSOCIATED CONTENT

Supporting Information

The Supporting Information is available free of charge at https://pubs.acs.org/doi/10.1021/acs.jpcc.5c03044.

Experimental procedures, characterization, data evaluation, and computational work (PDF)

https://doi.org/10.1021/acs.jpcc.5c03044
J. Phys. Chem. C 2025, 129, 14167−14176

AUTHOR INFORMATION

Corresponding Author

Angela Möller − *Department of Chemistry, Johannes Gutenberg-University Mainz, 55128 Mainz, Germany;* orcid.org/0000-0002-3323-6998; Email: angela.moeller@uni-mainz.de

Authors

Marcel Dürl − *Department of Chemistry, Johannes Gutenberg-University Mainz, 55128 Mainz, Germany*

Ruiwen Xie − *Institute of Materials Science, TU Darmstadt, 64287 Darmstadt, Germany*

Martin Panthöfer − *Department of Chemistry, Johannes Gutenberg-University Mainz, 55128 Mainz, Germany*

Hongbin Zhang − *Institute of Materials Science, TU Darmstadt, 64287 Darmstadt, Germany*

Complete contact information is available at: https://pubs.acs.org/10.1021/acs.jpcc.5c03044

Notes

The authors declare no competing financial interest.

ACKNOWLEDGMENTS

This work was funded by the Deutsche Forschungsgemeinschaft (DFG, German Research Foundation)—CRC 1487, "Iron upgraded!"—Project Numbers 443703006 and 442589410. The authors gratefully acknowledge computing time at the NHR Center NHR4CES at RWTH Aachen University (Project Numbers 20454 and 24007), funded by the Federal Ministry of Education and Research, and the state governments participating on the basis of the resolutions of the GWK for National High-Performance Computing at universities (www.nhr-verein.de/unsere-partner). We thank Chen Shen for technical support.

REFERENCES

(1) Rank, M.; Franke, P. L.; Seifert, H. J. Thermodynamic investigations in the Al−Fe system: Thermodynamic modeling using CALPHAD. *Int. J. Mater. Res.* **2019**, *110*, 406−421.

(2) Sundman, B.; Ohnuma, I.; Dupin, N.; Kattner, U. R.; Fries, S. G. An assessment of the entire Al−Fe system including $D0_3$ ordering. *Acta Mater.* **2009**, *57*, 2896−2908.

(3) Okamoto, H. Al-Mo (Aluminum-Molybdenum). *J. Phase Equilib. Diffus.* **2010**, *31*, 492−493.

(4) Kriegel, M. J.; Walnsch, A.; Fabrichnaya, O.; Pavlyuchkov, D.; Klemm, V.; Freudenberger, J.; Rafaja, D.; Leineweber, A. High-temperature phase equilibria with the bcc-type β (AlMo) phase in the binary Al−Mo system. *Intermetallics* **2017**, *83*, 29−37.

(5) Bahetia, V. A.; Raju, R. Interdiffusion study of the topologically closed packed μ phase and the phase boundary compositions in the Fe−Mo system. *Intermetallics* **2019**, *113*, No. 106586.

(6) Yannello, V. J.; Fredrickson, D. C. Generality of the 18-n Rule: Intermetallic Structural Chemistry Explained through Isolobal Analogies to Transition Metal Complexes. *Inorg. Chem.* **2015**, *54*, 11385−11398.

(7) Vinokur, A. I.; Fredrickson, D. C. 18-Electron Resonance Structures in the BCC Transition Metals and Their CsCl-type Derivatives. *Inorg. Chem.* **2017**, *56*, 2834−2842.

(8) Eumann, M.; Sauthoff, G.; Palm, M. Phase equilibria in the Fe−Al−Mo system−Part II: Isothermal sections at 1000 and 1150°C. *Intermetallics* **2008**, *16*, 834−846.

(9) Raghavan, V. Al-Fe-Mo (Aluminum-Iron-Molybdenum). *J. Phase Equilib. Diffus.* **2009**, *30*, 372−374.

(10) Du, Z.; Guo, C.; Li, C.; Zhang, W. Thermodynamic Description of the Al-Mo and Al-Fe-Mo Systems. *J. Phase Equilib. Diffus.* **2009**, *30*, 487−501.

(11) Sodré, N.; Guillermo Gonzales-Ormeño, P.; Petrilli, H. M.; Schön, C. G. Ab initio calculation of the BCC Fe−Al−Mo (Iron−Aluminum−Molybdenum) phase diagram: Implications for the nature of the τ_2 phase. *Calphad* **2009**, *33*, 576−583.

(12) Fartushna, I.; Witusiewicz, V.; Samelyuk, A.; Bulanova, M. Thermodynamic re-modeling of the binary Al−Mo and ternary Al−Fe−Mo systems based on novel experimental data. *J. Mater. Sci.* **2024**, *59*, 18159−18195.

(13) Oster, M.; Ksenofontov, V.; Dürl, M.; Möller, A. Giant Negative Magnetization in $Al_{9-x}Fe_xMo_3$. *Chem. Mater.* **2019**, *31*, 9317−9324.

(14) Leineweber, A.; Kriegel, M. J.; Distl, B.; Martin, S.; Klemm, V.; Shang, S.-L.; Liu, Z.-K. An orthorhombic $D0_{22}$-like precursor to Al_8Mo_3 in the Al−Mo−Ti system. *J. Alloys Compd.* **2020**, *823*, No. 153807.

(15) Coelho, A. *Topas Academic V7*; Coelho Software: Brisbane, 2020.

(16) Cheary, R. W.; Coelho, A. A fundamental parameters approach to X-ray line-profile fitting. *J. Appl. Crystallogr.* **1992**, *25*, 109−121.

(17) Stephens, P. Phenomenological model of anisotropic phase broadening in powder diffraction. *J. Appl. Crystallogr.* **1999**, *32*, 281−289.

(18) Lagarec, K. *D. R. Recoil - Mössbauer spectral analysis software for Windows*; Department of Physics, University of Ottawa: Ottawa, ON, 1998.

(19) Vitos, L. Total-energy method based on the exact muffin-tin orbitals theory. *Phys. Rev. B* **2001**, *64*, No. 014107.

(20) Perdew, J. P.; Burke, K.; Ernzerhof, M. Generalized gradient approximation made simple. *Phys. Rev. Lett.* **1996**, *77*, 3865.

(21) Soven, P. Coherent-potential model of substitutional disordered alloys. *Phys. Rev.* **1967**, *156*, 809.

(22) Gyorffy, B.; Pindor, A.; Staunton, J.; Stocks, G.; Winter, H. A first-principles theory of ferromagnetic phase transitions in metals. *J. Phys. F: Met. Phys.* **1985**, *15*, 1337.

(23) Savin, A.; Nesper, R.; Wengert, S.; Fässler, T. F. ELF: The electron localization function. *Angew. Chem., Int. Ed.* **1997**, *36*, 1808−1832.

(24) Maintz, S.; Deringer, V. L.; Tchougréeff, A. L.; Dronskowski, R. LOBSTER: A tool to extract chemical bonding from plane-wave based DFT. *J. Comput. Chem.* **2016**, *37*, 1030−1035.

(25) Lamorgese, A.; Mauri, R. Spinodal decomposition of chemically reactive binary mixtures. *Phys. Rev. E* **2016**, *94*, No. 022605.

(26) Bertei, A.; Chueh, C.-C.; Mauri, R. Dynamics of phase separation of sheared binary mixtures after a nonisothermal quenching. *Phys. Rev. Fluids* **2021**, *6*, No. 094302.

(27) Miller, G. J.; Li, F.; Franzen, H. F. The structural phase transition in calcium-aluminum compound ($CaAl_4$): a concerted application of Landau theory and energy band theory. *J. Am. Chem. Soc.* **1993**, *115*, 3739−3745.

(28) Khachaturian, A. G. *Theory of structural transformations in solids*; John Wiley and Sons: New York, 1983.

(29) Staunton, J.; Gyorffy, B.; Pindor, A.; Stocks, G.; Winter, H. The "disordered local moment" picture of itinerant magnetism at finite temperatures. *J. Magn. Magn. Mater.* **1984**, *45*, 15−22.

(30) Pindor, A. J.; Staunton, J.; Stocks, G. M.; Winter, H. Disordered local moment state of magnetic transition metals: a self-consistent KKR CPA calculation. *J. Phys. F: Met. Phys.* **1983**, *13*, 979.

(31) Ruderman, M. A.; Kittel, C. Indirect Exchange Coupling of Nuclear Magnetic Moments by Conduction Electrons. *Phys. Rev.* **1954**, *96*, 99−102.

(32) Kasuya, T. A Theory of Metallic Ferro- and Antiferromagnetism on Zener's Model. *Prog. Theor. Phys.* **1956**, *16*, 45−57.

(33) Yosida, K. Magnetic Properties of Cu-Mn Alloys. *Phys. Rev.* **1957**, *106*, 893−898.

(34) Mydosh, J. A. Spin glasses: redux: an updated experimental/materials survey. *Rep. Prog. Phys.* **2015**, *78*, No. 052501.

(35) Jeudy, V.; Díaz Pardo, R.; Savero Torres, W.; Bustingorry, S.; Kolton, A. B. Pinning of domain walls in thin ferromagnetic films. *Phys. Rev. B* **2018**, *98*, No. 054406.
(36) Liu, M.; Du, S.; Wang, F.; Adam, R.; Li, Q.; Ma, X.; Guo, X.; Chen, X.; Yu, J.; Song, Y.; et al. Influence of surface pinning in the domain on the magnetization dynamics in permalloy striped domain films. *J. Alloys Compd.* **2021**, *869*, No. 159327.
(37) Gopal, E. S. R. Chapter Electronic Specific Heat. In *Specific Heats at Low Temperatures*; Springer: Boston, MA, 1966; pp 55−83.
(38) Van der Kraan, A.; Buschow, K. The ^{57}Fe Mössbauer isomer shift in intermetallic compounds of iron. *Phys. B+C* **1986**, *138*, 55−62.
(39) Gütlich, P.; Bill, E.; Trautwein, A. X. *Mössbauer spectroscopy and transition metal chemistry: Fundamentals and applications*; Springer-Verlag, 2011; p 568.

https://doi.org/10.1021/acs.jpcc.5c03044
J. Phys. Chem. C 2025, 129, 14167−14176